Creep Properties of Shale and Predicted Impact on Proppant Embedment for the Caney Shale, Oklahoma

Margaret Benge[1], Allan Katende[2], Jonny Rutqvist[3], Mileva Radonjic[2,4], Andrew Bunger[1,5 *]

[1] *University of Pittsburgh, Department of Civil and Environmental Engineering, Pittsburgh, PA, USA*

[2] *Oklahoma State University, Department of Chemical Engineering, Stillwater, OK, USA*

[3] *Lawrence Berkeley National Laboratory, Energy Geosciences Division, Berkeley, CA, USA*

[4] *Oklahoma State University, Boone Pickens School of Geology, Stillwater, OK, USA*

[5] *University of Pittsburgh, Department of Chemical and Petroleum Engineering, Pittsburgh, PA, USA*

*** Corresponding Author:**

Andrew Bunger, University of Pittsburgh, Email: Bunger@Pitt.edu

Accepted Version of Manuscript Published as

Benge M., Katende A., Rutqvist J., Radonjic M., and Bunger A. Creep Properties of Shale and Predicted Impact on Proppant Embedment for the Caney Shale, Oklahoma. Rock Mechanics and Rock Engineering, 56, 5903–5921 (2023) https://doi.org/10.1007/s00603-023-03362-8.

Abstract

The Caney shale is an emerging hydrocarbon play located in southwest Oklahoma, USA. Within the Caney shale exist facies which were initially dubbed “reservoir” and “ductile” based on evaluation of well logging data. While past work has shown the distinction of “brittle” and “ductile” is not mechanically justifiable according to formal definitions, the current work shows some important differences between nominally ductile and reservoir zones. First, the “ductile” zones are more clay rich and have textural differences which can be expected to lead to differences in mechanical properties. One important impact of these differences is observed in triaxial creep experiments showing the “ductile” zones are more prone to creep deformation. Numerical simulations predict the “reservoir” zones will experience very little proppant embedment due to creep deformation of hydraulic fractures around proppant particles. On the other hand, “ductile” zones can be expected to undergo creep-driven proppant embedment leading to loss of fracture aperture ranging up to 100% loss, depending upon the spatial density of the proppant distribution. Hence, this research shows the identification of nominally “ductile” zones from well logs, while a misnomer, can be useful in finding clay-rich, creep-prone zones which will be the most prone to proppant embedment and hence vulnerable to greater production decline over time.

Key Words: Shale, Creep, Modeling, Fracture Closure, Proppant Embedment

1. Introduction

Located in southern Oklahoma below the Springer shale and above the Woodford shale, the Caney is an emerging shale play under examination for hydrocarbon production (Cardott, 2017). A high clay content and the increased potential for ductile behavior in some segments of the formation imply this shale formation may be more difficult to produce than other shale plays currently in production. Although Caney vertical core does have regions where clay content is sufficiently lower, this is compensated by an additional presence of carbonates and quartz (Awejori et al, 2021, Radonjic et al, 2020, and Wang et al, 2021). With this zonation, it can be proposed to distinguish some subunits within the Caney as "ductile", and other subunits as nominally more "brittle" and hence more promising as "reservoir" rocks. However, previous research work has shown the Caney is not "ductile" according to the traditional brittle/ductile definitions in rock mechanics (Benge et al., 2021). Nonetheless, despite the fact this labeling is a misnomer, distinguishing "brittle" and "reservoir" zones has practical relevance, especially as it is able to label zones as relatively stronger/weaker (Benge et al., 2021) and more susceptible to creep deformation over time, as is the focus of this present work.

The creep deformation associated with the "ductile" zones has clear connections to the effectiveness of formation stimulation through hydraulic fracturing, most notably due to its impact on the distribution of in-situ stresses (see Sone and Zoback, 2014), the closure of fractures over time, and the embedment of proppant material (see review of Bandara, 2019, Katende et al, 2021a, and Frash et al, 2019). In this paper, we focus on the impact of creep on proppant embedment, using elasto-viscoplastic simulations to predict five-year proppant embedment to contrast a "reservoir" zone which undergoes little creep deformation with a "ductile" zone which is highly prone to creep deformation. Hence, this work provides not only predictions specific to the Caney, but also provides an illustrative test case showing how subunits within a reservoir can behave very differently depending on their geomechanical properties in general and their propensity to undergo creep in particular. While the conclusions presented in this paper are limited by the number of available samples, the methodology aims to provide a framework for full characterization of formations including mineralogical analysis, triaxial testing, and creep testing.

Simulations of creep-accommodated proppant embedment require experimental characterization. For this reason, the present work entails creep compliance testing under triaxial loading conditions and at elevated temperatures approximating those relevant to reservoir conditions. The multi-stage creep compliance tests are

modified from Rassouli and Zoback (2018), and the data is shown to lend itself to a power-law creep model which is readily implemented in the numerical simulations. Samples are tested from three nominal "reservoir" zones and two nominal "ductile" zones, enabling comparison and contrasting of these zones in terms of their propensity for creep deformation.

Besides the testing of creep properties and connecting these to predictions of proppant embedment, there are additional connections of interest to the present work. The first is to examine the effectiveness of well-log based identification of nominally "reservoir" and "ductile" zones to determine the sections of the reservoir which are most promising for sustained production. The second is to examine the differences in mineralogy and microstructure among the identified zones. Ties can therefore be proposed both to mineralogy (for example clay content and/or organic content) and to the fact the same quantity of minerals can occupy the rock volume differently. This microstructure takes into account the internal architecture of the rock matrix, where porosity and natural fractures also contribute to how rock may respond to physical and/or chemical changes at different spatial and temporal scales (Wang et al. 2021). Hence, the present work includes a detailed description of both mineralogy and microstructure because it is ultimately a key factor in determining the macroscopic properties measured in mechanical tests and considered by the numerical simulations. Furthermore, by providing an integrated case study of connections among log-derived properties, mineralogy, microstructure, creep, and predicted tendency for proppant embedment, the present work can be relevant not only to the Caney shale, but also can provide an illustrative case to act as a template for similar studies on other formations.

By way of organization, this paper firstly describes the core and the exploration well from which it was extracted. It then identifies five formation subunits as either "reservoir" (expected to be more brittle) or "ductile" based on the elastic properties as determined by the well log. Next, samples obtained from the core are described in terms of context, meso/micro-scale structures, mineralogy, and triaxial strength. These all provide the context by which mechanical properties can be different among the various zones. The paper then focuses on creep compliance tests, showing the differences from each zone and providing a power-law description of creep unique to each zone to be used in numerical simulations. Finally, taking characterization from the mechanical testing, an elasto-visco-plastic mechanical model is used to predict proppant embedment, thus providing the backdrop to a closing discussion of the synthesis of log data, mineralogy, microstructure, mechanical testing, and numerical simulation for predicting the

most promising and most problematic zones within a reservoir from the perspective of sustaining production through propped hydraulic fractures.

2. Core Description

2.1. Well Location and Sampling Program

The Caney Shale is located in the Arkoma basin in southern Oklahoma, USA. A recent exploration well (completed in February 2020 and described in more detail by Katende et al, 2023) intersected approximately 500 feet of the Caney formation. The formation characterization began with determining petrophysical properties from an open-hole well log. Five zones of interest were identified based on these properties, most notably the Poisson's ratio but also including electrical resistivity and gamma ray radiation. From shallowest to deepest, the zones were identified as Reservoir 1 (R1), Ductile 1 (D1), Reservoir 2 (R2), Ductile 2 (D2), and Reservoir 3 (R3), as shown along with well log data in Fig. 1. For the purpose of naming, the "reservoir" zones have a Poisson's ratio less than 0.25 (indicated by yellow shading in Fig. 1), have a low gamma, and have a high resistivity. Note a low value of Poisson's ratio has been associated with microseismically "brittle" zones in the past (e.g., Rickman et al., 2008) while low gamma and high resistivity are typically associated with low clay content (see for example Fadjarijanto et al, 2018) which, in turn, is considered to be associated with higher brittleness (e.g. Bai, 2016).

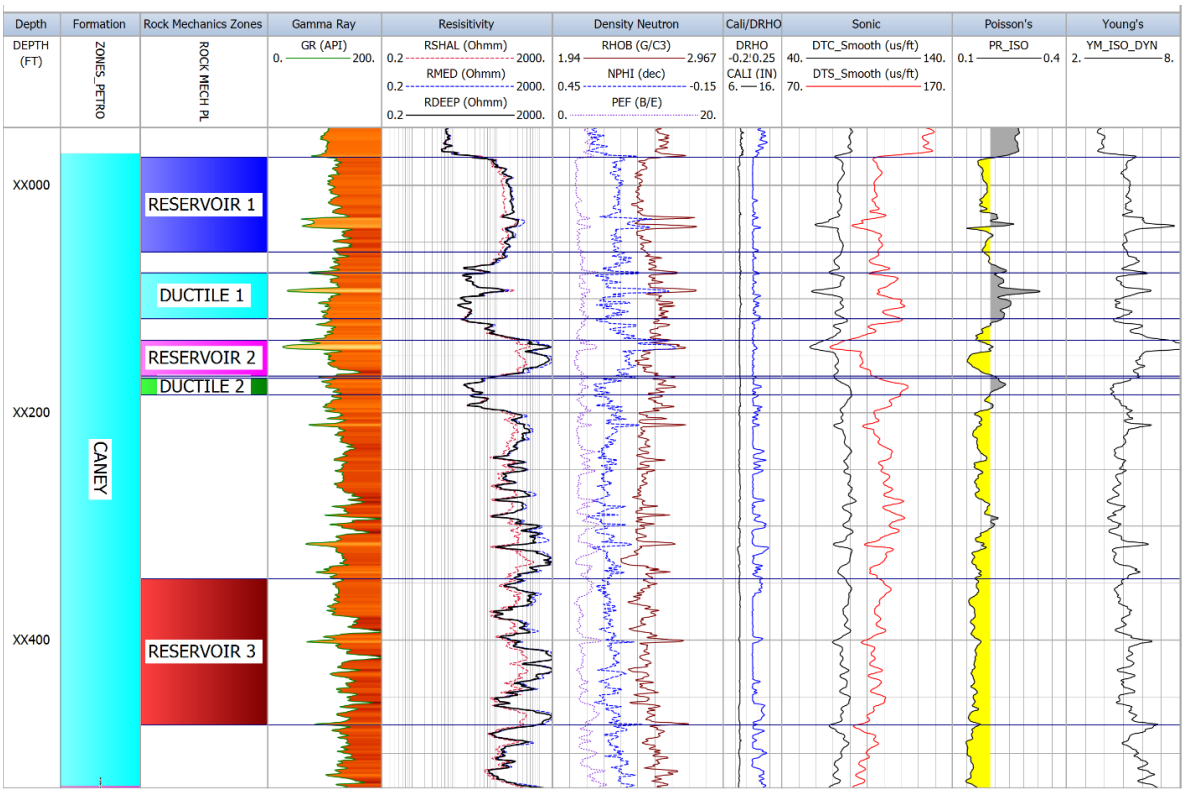

Fig. 1 Well log with identified zones indicated by different colored name boxes, note the variation in Poisson's ratio between the ductile and reservoir zones

In total, 650 feet of four-inch core was retrieved from the 2020 exploration well. From this four-inch core, cylindrical samples ("core plugs") were obtained from each of the five zones. The core plugs have dimensions 1.20 inches diameter by 2.36 inches long (30 mm diameter by 60 mm length). While multiple orientations of core plugs were taken, here we focus on results obtained from plugs with the main axis perpendicular to bedding planes (vertical core plugs). After the ends were surfaced to create parallel faces, samples were CT scanned to identify any flaws or de-bonding of bedding planes prior to preparing the samples for testing.

In addition to providing quality control for triaxial and creep testing, CT images of the samples can provide an idea of bulk heterogeneity. The bright white carbonate and pyrite grains in the sample-scale CT scans of Fig. 2 are contrasted by the darker fine-grained clay matrix. While the industrial CT scanner used in these images lacks sufficient resolution to depict microstructural features such as nano porosity, these values can be obtained using other methods such as scanning microscopy. Unfortunately, the resolution of the CT scanner was unable to show a clear distinction

between the nominally brittle and nominally ductile zones, and there were no significant differences between the zones when viewing the core without the use of any visual enhancements.

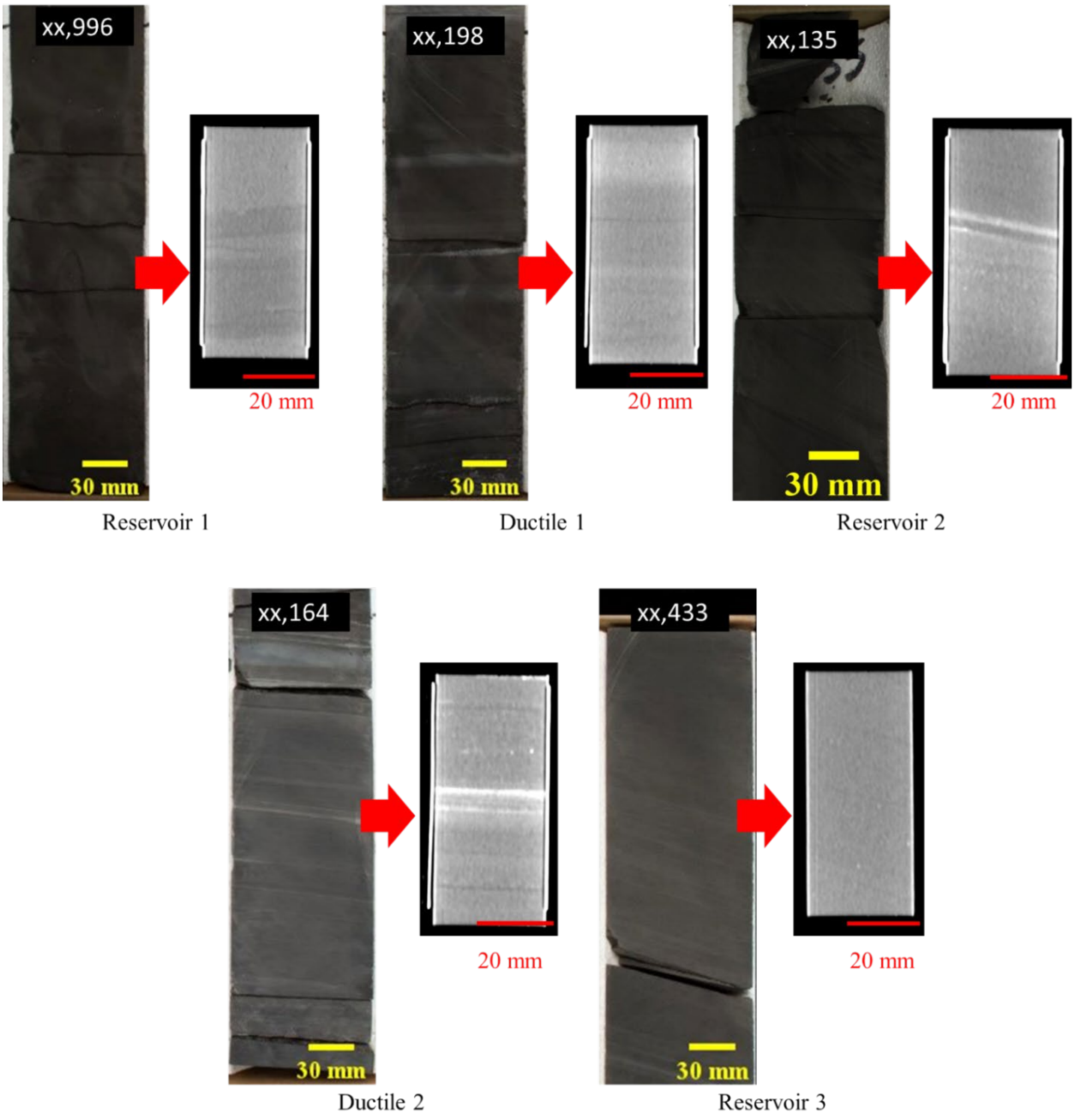

Fig. 2 Photographic images of the section of 4 inch core that was sampled by core plugging for each zone along with X-ray computer tomography scans of example 1.2 inch diameter core plugs used for quality control during sample preparation

Although minor partings can be observed on bedding planes and R2 and D2 are shown to have more variation in density among layers, Fig. 2 shows the samples are overall intact and lack pre-existing fractures at orientations which would be prone to slippage under triaxial loading. Prior to testing, samples were stored in sealed bags and while a small amount of surface drying may have occurred during experimental setup, the samples are treated to be at an "as received" saturation level.

2.2 Mineralogy and Microstructure

For geomechanical testing, proppant embedment, and characterization, samples were selected from the same zones as identified previously. In addition, XRD analysis was completed on 120 core samples across the approximately 650 feet of available core. Eight horizontal plugs were drilled from the Reservoir 3 zone and thin sections were made from 180 locations. The inherent inhomogeneity present in all sedimentary rocks was accounted for by averaging multiple measurements from samples located throughout the five zones of interest.

At each of the selected zones shown in Fig. 1, two grams of crushed rock powder were used to identify the bulk mineral composition with a Bruker D8 Advanced X-ray Diffraction (XRD) instrument at Oklahoma State University Laboratory which is coupled with a Lynxeye detector. Each sample was scanned from 5 to 80 degrees 2-theta angle with 0.01 degree step and dwell time of 0.5 seconds. Semi-quantitative analyses were obtained using the Bruker's Diffrac.suite eva. As can be observed in Fig. 3, the mineralogical composition of these Caney samples matches what was observed from petrophysical well logs, with the reservoir sections (R1, R2, and R3) having low clay content (18, 25 and 13 wt%) and relatively high carbonate content (14, 19 and 26 wt%), and clearly separating the Reservoir 3 (R3) region as the most favorable for fracturing and subsequent hydrocarbon production based on the criteria determined using the well log.

Moving beyond mineralogy, the microstructural characterization entails obtaining 1 inch diameter by 0.5 inch high disc-like samples from each zone. These were polished and coated with carbon prior to scanning electron microscopy (SEM) analysis for elemental mapping and back scatter electron micrographs. To avoid clay-water interaction, a specially designed protocol was developed for polishing, using an Allied HighTech multiprep polisher to prepare flat sample surfaces for SEM imaging. First a 600 grit silicon carbide abrasive disc was used for grinding to remove initial roughness. After each step, the surfaces were inspected under the microscope to ensure a uniform polished pattern. Grinding-induced deformations were removed using 6 µm diamond suspension on gold label

polishing cloth and 1 µm diamond suspension on white label polishing cloth, with purple lube. To avoid the water-sensitivity of shale samples, the commercial lubricant sold as Purple Lube was used. Purple Lube is a low viscosity, ethyl alcohol-based polishing lubricant. The final polishing was achieved with 0.05 µm water-free colloidal silica suspension used on a Chem-Pol polishing cloth. Polished samples were then dried in an oven at 50 °C before a conductive coating was applied prior to SEM/EDS analysis.

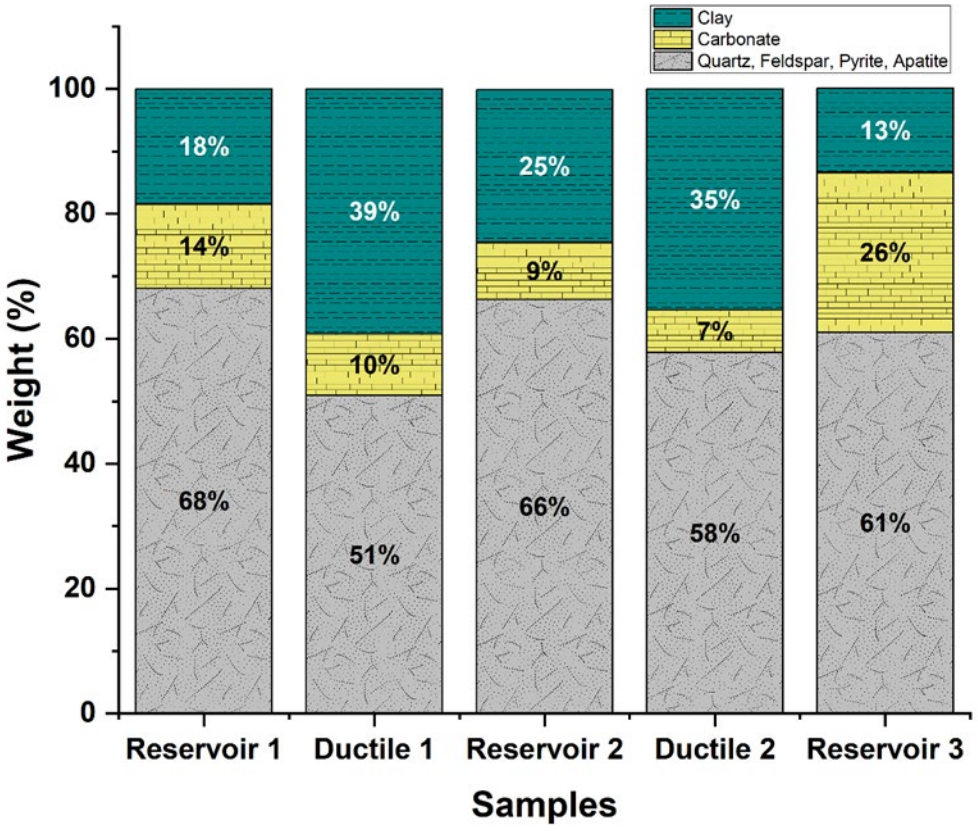

Fig. 3 Mineralogical composition of the Caney shale samples in the identified zones

SEM imaging was then carried out using an FEI Quanta 600 field-emission gun Environmental Scanning Electron Microscope in both backscattered and secondary electron mode. The elemental mapping and spot mode analysis were obtained using a Bruker EDS X-ray microanalysis system. SEM images and spectra were obtained at 20 kV and various magnifications, from a larger field of view to a higher magnification to reveal the characteristics of interfaces and surface properties of various phases. Scanning electron microscopy determines the two-dimensional spatial distribution of inorganic (mineral) and organic (kerogen) content and the presence of porosity and micro

fractures. Fig. 4 through Fig. 8 show the microstructural characterization of each zone. Chemical elemental maps were obtained using EDS, primarily to provide an insight into the degree of compositional heterogeneity in each of the five zones. The as-received samples from reservoir and ductile zones differ primarily in grain size, porosity, and composition, as is to be expected due to the difference in depth due to the different depositional environment and the impact of geological activities related to uplifting and fluid migration over geological times. A specific examination of each zone provides insight into the unique properties of each sample.

The Reservoir 1 sample shown in Fig. 4 provides an average 350 by 300 µm field view, a medium range resolution capable of capturing the compositional arrangement, micro-porosity, and micro fractures of the sample. The sample shown is rich in quartz and carbonates and has large conglomerations of pyrite well distributed in the matrix of clays. This characteristic is seen in the overlapping of aluminum and silica elemental maps. The black areas in the images represent organic matter with a sponge-line appearance because the porosity is not fully resolved at the displayed magnification. Additionally, the large dolomite, calcite, and pyrite aggregated into large multigrain nodules which contribute to the difference in geomechanical and geochemical behavior during stimulation compared to the ductile zones which will be shown to have a much finer grained clay matrix.

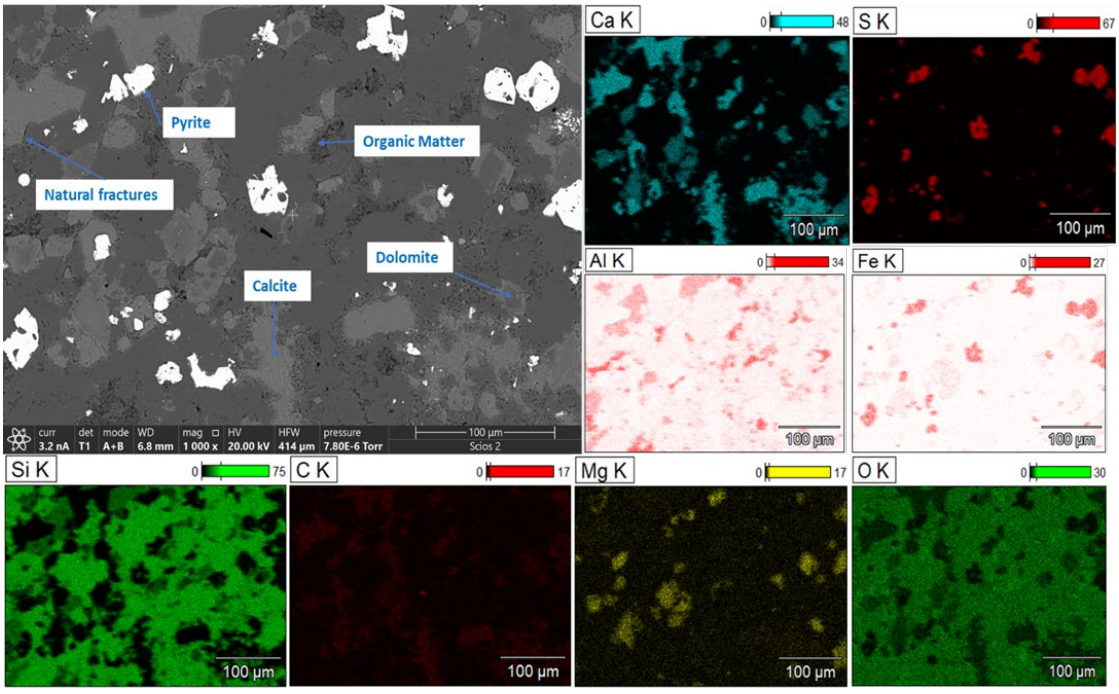

Fig. 4 Reservoir 1 SEM Backscatter Electron (BSE) micrographs at 20 kV and 1000 X magnification

The Ductile 1 image in Fig. 5 shows how clay and fine-grained silt dominate the sample, with the presence of fine-grained apatite depicted by bright white in the calcium maps and large diamond-shaped dolomite grains with calcified rims. Organic matter is present as small inclusions evenly dispersed throughout the sample. The micro fractures present are most likely an artifact of sample preparation. Finally, the aluminum and silica maps indicate some clays form thin lamellar structures, seen in bottom right of the figure.

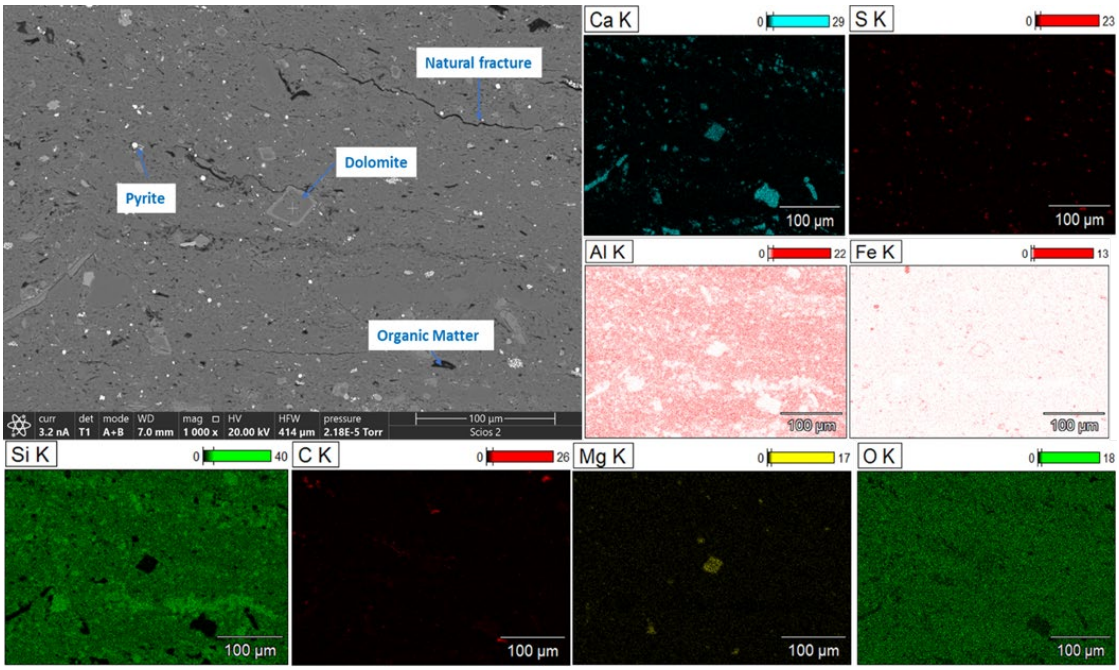

Fig. 5 Ductile 1 SEM Backscatter Electron (BSE) micrograph at 20 kV and 1000 X magnification

Fig. 6 demonstrates the more porous matrix of Reservoir 2, with calcite and dolomite embedded in the clay-rich matrix which appears to be swirled without clear layering. Organic matter is present both as coarse-grained isles and as very fine-grained matter interwoven in the clay matrix.

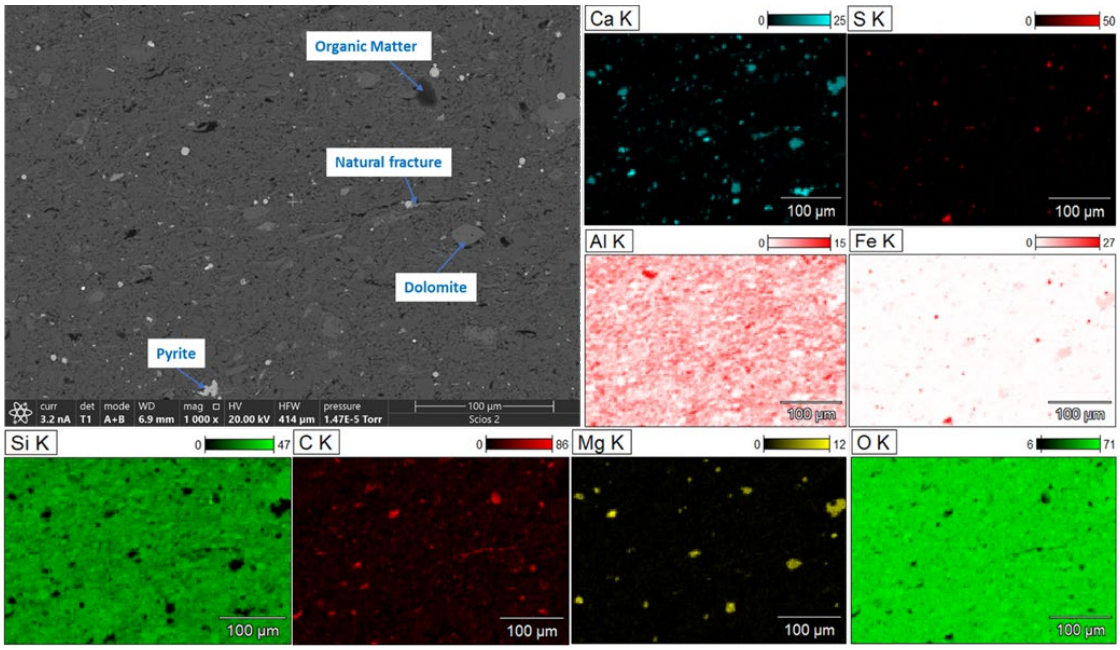

Fig. 6 Reservoir 2 SEM Backscatter Electron (BSE) micrograph at 20 kV and 1000 X magnification

The second ductile zone, Fig. 7, is similar to the first ductile zone and contains large individual dolomite grains within a fine-grained silt clay matrix. This sample also shows lens-like kerogen, indicating the presence of layering as seen when looking left to right in the figure 7.

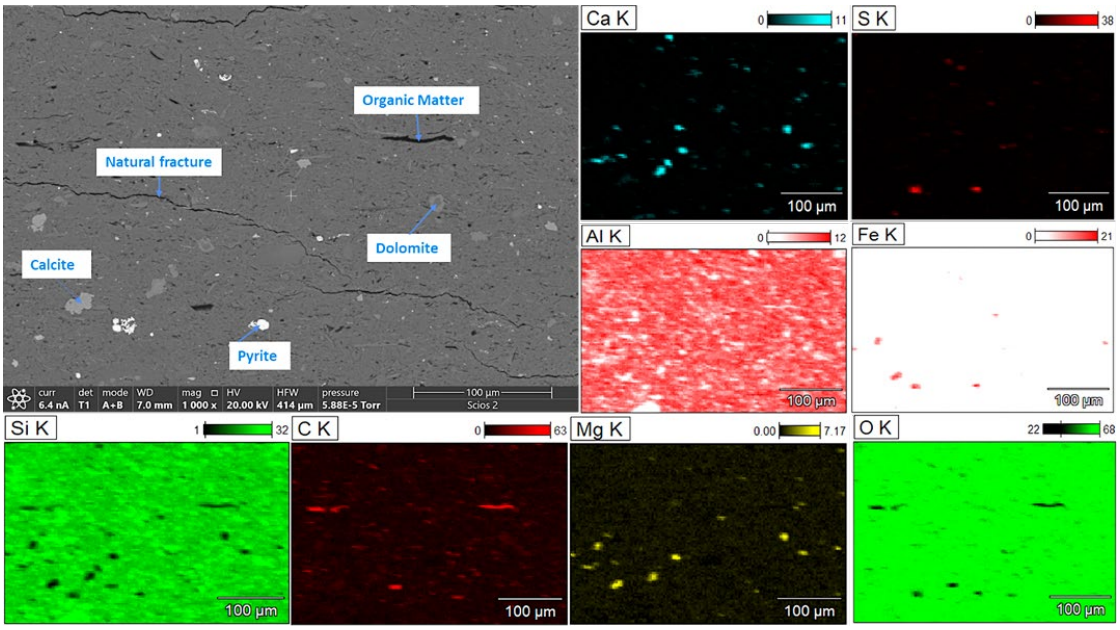

Fig. 7 Ductile 2 SEM Backscatter Electron (BSE) micrograph at 20k V and 1000 X magnification

Finally, Fig. 8 immediately stands out compared to all other zones. Reservoir 3 has a high kerogen content, indicating it is a favorable target for stimulation, with a texture which demonstrates a diagonal direction from the bottom left to the top right of the image. Pyrite does not adhere to the same directional preferences shown by the clays and kerogen. The calcium and magnesium maps depict a fine-grained dolomite present in the sample.

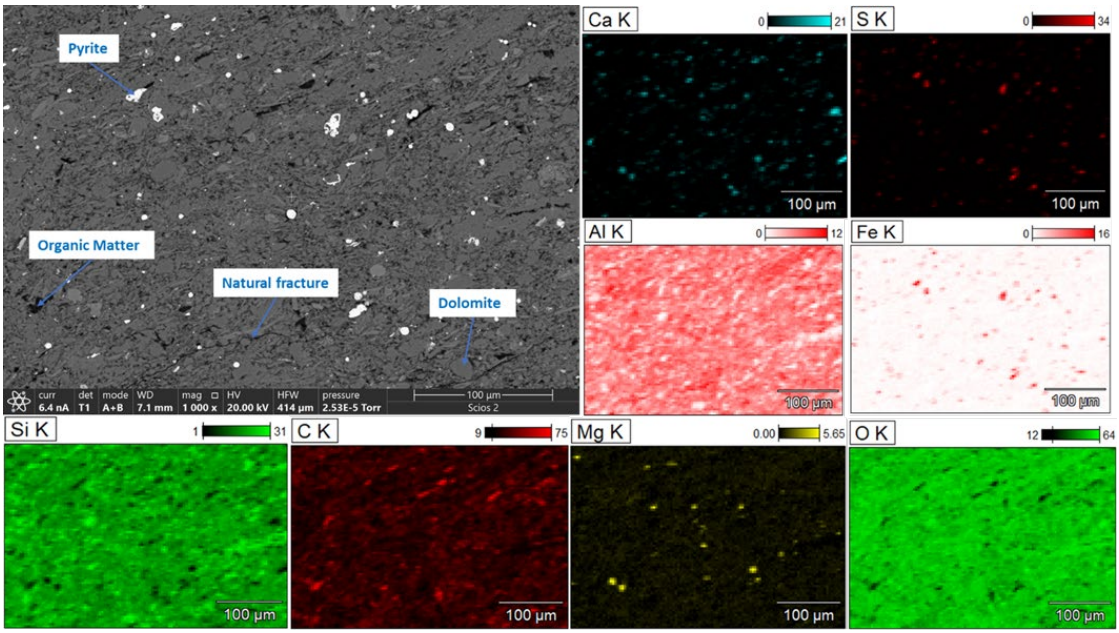

Fig. 8 Reservoir 3 SEM Backscatter Electron (BSE) micrograph at 20kV and 1000X magnification

The mineralogy in all SEM micrographs agrees with XRD data. The nominally more ductile samples show higher clay content than the nominally more brittle zones, and the opposite trend is observed for carbonates, which would contribute to how the rock responds to mechanical load tests as well as prolonged creep tests. The variation in XRD bulk mineralogical composition between the zones identified as nominally ductile and nominally brittle is clearly linked to the visual variation seen in the SEM images, where the black organic material is contrasted by the darker gray aluminosilicates and somewhat lighter gray carbonate, bright gray quartz, and bright white pyrite and apatite. Each of these mineral groups has different mechanical and chemical stability which could potentially be taken out of equilibrium because of drilling, completions and production (Awejori et al, 2022 and Xiong et al., 2022). Organic matter is not detectable in the XRD but the SEM micrographs and the EDS chemical elemental maps show the difference in the amount present as well as in the morphology of kerogen, which is present in ductile zones as fine grained and well dispersed, compared to the larger lens-like shapes of kerogen in reservoir zones with a sponge-like texture indicating kerogen porosity. Note a similar correlation has been previously observed in other shale characterization efforts, as discussed by Loucks et al (2012).

3. Rock Mechanical Properties

Previous rock mechanics testing under ambient conditions showed the nominally ductile zones have lower tensile strength, lower unconfined compressive strength, and lower fracture toughness compared to the nominally brittle reservoir zones (Benge et al., 2021). This prior work also presents results of triaxial testing. However, for completeness, it is necessary to reiterate the triaxial testing procedure and results as they are relevant to the simulations presented later in this paper. Vertical core samples drilled perpendicular to bedding planes were subjected to single stage triaxial tests at 90 °C and confining pressures ranging from 50-3000 psi (3.4-20.7 MPa), with the method based on ASTM 7012-14 (2014). A polymer sleeve surrounded the sample to allow application of radial confinement while preventing oil intrusion into the pore spaces of the rock. The sample and sleeve were placed in a Hoek-type triaxial cell (see Fig. 9). Confinement in the radial direction was applied to the sample by pressurizing hydraulic oil in the Hoek cell using an ISCO syringe pump. Axial loading was provided by an Instron load frame with Partner control software. Heating tape was wrapped around the cell and an internal thermocouple used to measure the specimen temperature, as shown in Fig. 8. A BriskHeat SDX digital temperature controller was set to control temperature at 90 °C.

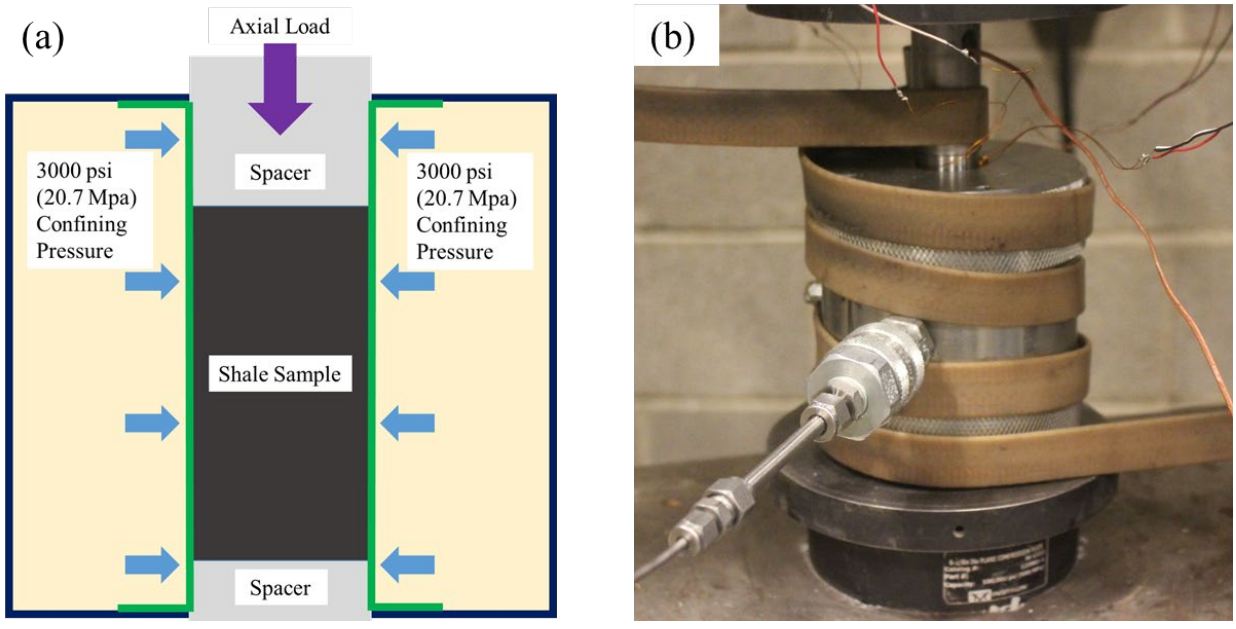

Fig. 9 (a) Diagram of Hoek triaxial cell experimental setup and (b) cell set in load frame with heating tape wrapped around cell (external LVDTs not shown)

Throughout testing, the axial load, confining pressure, sample temperature, axial strain, and radial strain were monitored. The axial load was measured using the load cell in the Instron load frame while the confining pressure was controlled from the ISCO pump controller. As previously indicated, the BriskHeat controller maintained a constant temperature during the test, which was verified by measurement from a thermocouple placed between the jacket and the top loading platen, as close to the specimen as possible. Finally, axial and radial strains were measured using strain gauges adhered to the sample with an adhesive and recorded using a Vishay strain recorder.

To perform experiments, a confining radial pressure was applied to the jacketed sample along with an equivalent axial load in order to start the test under hydrostatic conditions. This initial hydrostatic confinement was held at 500 psi (~3.4MPa) as the temperature was increased, except in low confinement triaxial tests when the targeted testing confinement value was 500 psi, in which case the hydrostatic load was set to 250 psi. Once the sample reached 90 °C, the axial load and confining pressure were increased in unison with the hydrostatic pressure required for the test. The sample remained at the target temperature and pressure for approximately two hours to ensure equilibrium of temperature and to enable drainage of any pore pressure generated during the confining and heating stages. Once at equilibrium, a single-stage ramp in the axial loading commenced, loading the sample via a constant axial displacement rate of 0.2 mm/min (0.008 in/min) until failure was detected through a decrease or flattening in the measured axial load. As soon as evidence of failure was detected the experiments were stopped and no attempt was made to capture post-peak behavior. This is because the specialized membranes used in this type of triaxial cell were very prone to failure during the post-peak time, especially at the temperatures used for these tests. Furthermore, even if the membrane did not fail, continuing to load into the post-peak range had the tendency to cause the specimen to become permanently lodged in the membrane so the sample and/or the membrane had to be destroyed in order to remove the sample for post-test documentation and storage.

Stress-strain curves for samples tested at 3000 psi (20.7 MPa) confining pressure are presented in Fig. 10. As can be seen by the axial strain lines, the ductile zones do not display a significantly different slope than the reservoir zones. Computing the slope gives the Young's modulus, which is indicated in Fig. 11 for each zone and is observed to have no systematic correlation with the distinction of "reservoir" or "ductile", per se, although Ductile 2 does have the smallest value. Similarly, all values of Poisson's ratio are in approximately the same range and display no clear difference between the nominally brittle and nominally ductile zones. This result for confined static Poisson's ratio

stands in contrast to the dynamic value of the Poisson's ratio from the well log in Fig. 1, which correlates strongly with zones for which a higher value is taken as one indication of whether a zone is nominally "ductile".

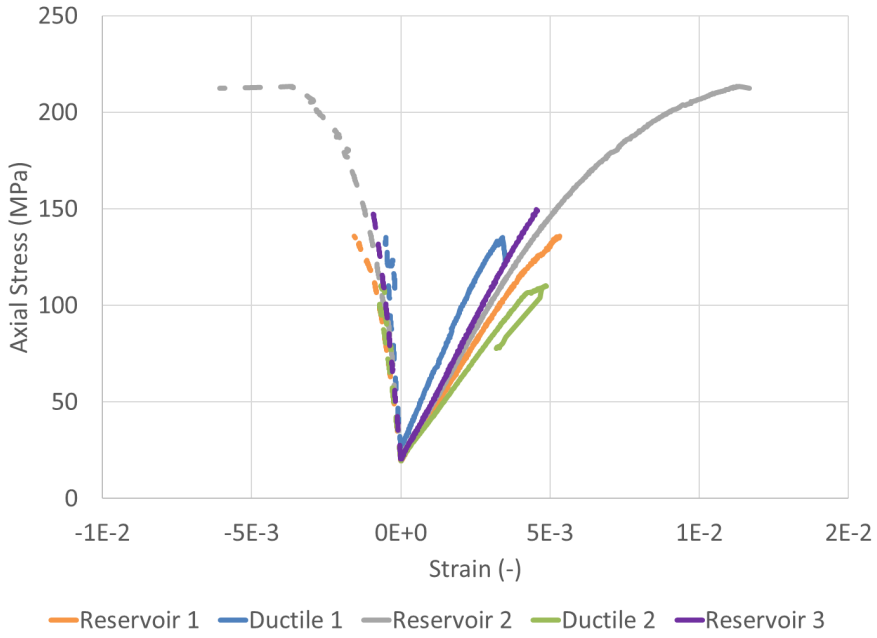

Fig. 10 Stress vs axial strain (solid) and radial strain (dashed) for 3000 psi confined (20.7 MPa) samples

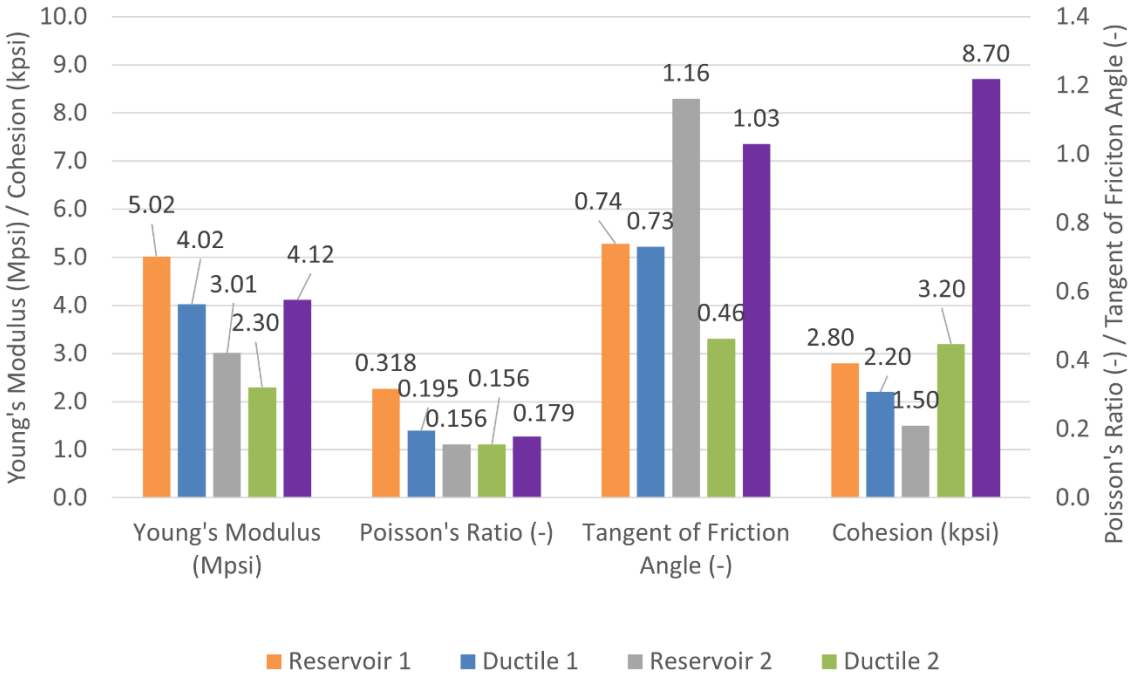

Fig. 11 Average Young's modulus (Mpsi), average Poisson's ratio (-), tangent of friction angle (-), and cohesion (kpsi) for each zone as calculated from triaxial results

The maximum axial stress at failure, taken at a variety of confining stresses, is presented for each zone in Fig. 12. At nearly every confining level (except for the lowest value, intended to approximate an unconfined compressive strength at 90 ºC), the two ductile zones are the weakest. These results can also be used to calculate the cohesion c and friction angle ϕ using (Kovari et al, 1983)

$$\Phi = sin^{-1}\frac{m-1}{m+1} \qquad c = b * \frac{1-sin\,\Phi}{2*cos\,\Phi} \tag{1}$$

Here m and b are the slope and y-intercept of a linear fit to each curve in Fig. 12, represented as the dashed lines between points. The resulting values of cohesion and the curve of the friction angle are presented in Fig. 11. To make the axis scale more convenient, we present the friction coefficient the tangent of the friction angle. Here the most striking result is Ductile 2 clearly has the lowest value of the friction angle.

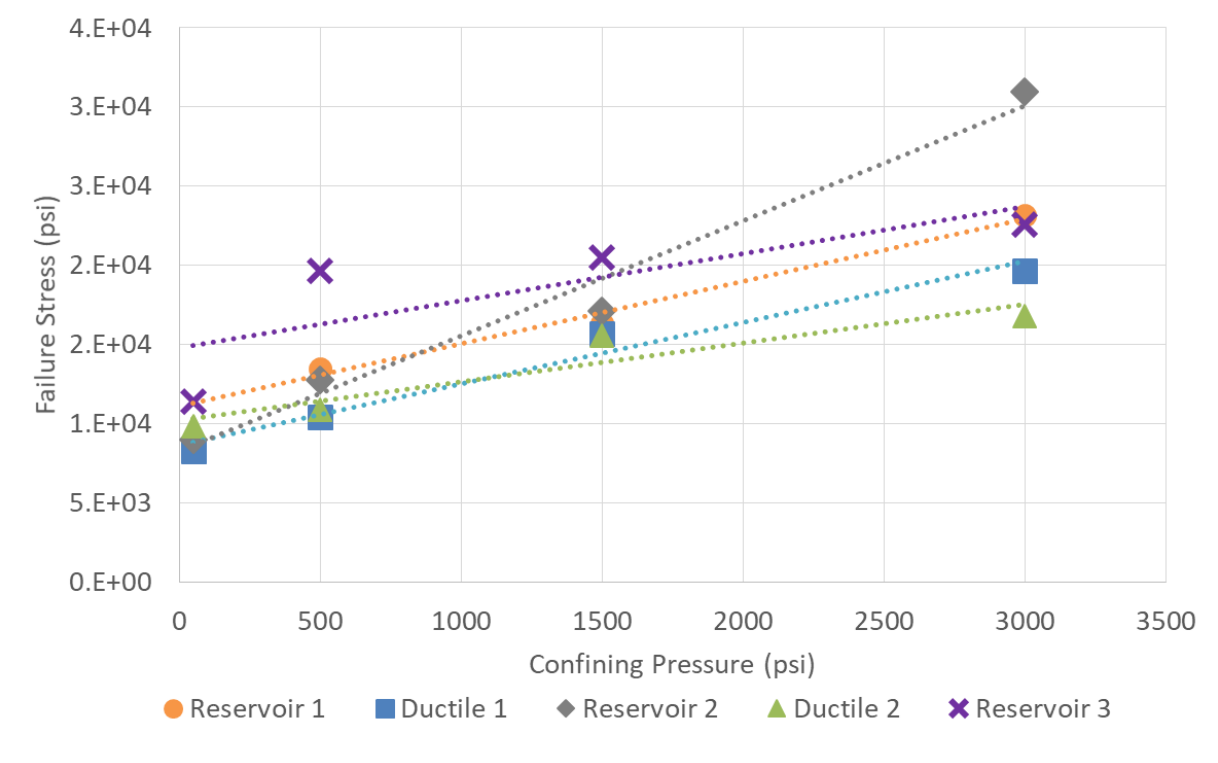

Fig. 12 Axial stress for each zone at various confining pressures with linear fit shown to calculate friction angle and cohesion

4. Creep Compliance

Creep testing was carried out using the same sample preparation and cell as for the triaxial testing. The equipment to control the temperature and pressure as well as monitor the strain was the same with the addition of external LVDTs to measure axial displacement of the sample monitored through an external DATAQ system. These were added because calibration tests indicated the attached strain gauges undergo some creep, probably in the adhesive, over long periods of time at 90 °C. Even with the use of high-temperature adhesives, it was not possible to remove this small amount of gauge creep. The LVDTs, in contrast, were very reliable over the long term. Additionally, the axial load frame was switched to an MTS 810 owing to superior long-term load control.

The applied confining pressure for all tests was 3000 psi (20.7 MPa) and the test temperature was 90 °C. Inspired by the approach of Rassouli and Zoback (2018), a multiple stage, fixed load procedure was developed. As before, a lower confining pressure of 500 psi (3.4 MPa) was maintained while the sample reached the 90 °C testing temperature. After reaching the test temperature the hydrostatic pressure was increased to 3000 psi (20.7 MPa). The hydrostatic pressure was maintained for at least 24 hours as the sample equalized, and the stabilized strain values were used as a reference point for the strain values for the remainder of the test (i.e., these are taken as the zero point in all the results reported subsequently in this paper). After the hydrostatic stage, the axial force was increased to 30% of the expected axial stress at failure for the sample when tested at a confining pressure 3000 psi (20.7 MPa) based on the results shown in Fig. 12. This increased load was maintained for twenty minutes before the sample was returned to hydrostatic conditions for another twenty minutes to monitor recovery. A second axial load step to the same level was held for twelve hours, with an accompanying twelve-hour relaxation stage. After a second twelve-hour loading stage, a two-hour recovery stage was used before the final axial load, again to 30% of expected load for failure, was applied for 72 hours. For reference, the expected maximum stress and the applied axial stresses for each of the cases are provided in Table 1.

Table 1 Expected confined compressive strength at 3000 psi confinement, shown with applied axial stress during creep testing

Zone	Expected Confined Compressive Strength (psi / MPa)	Applied Axial Stress (psi / MPa)
Reservoir 1	19,500 / 134.45	5,850 / 40.33
Ductile 1	19,500 / 134.45	5,850 / 40.33
Reservoir 2	30,500 / 210.29	9,100 / 62.74
Ductile 2	15,900 / 109.63	5,100 / 35.16
Reservoir 3	22,500 / 115.13	6,750 / 46.54

The strain evolution for each sample is presented in Fig. 13. Note, however, each sample had a different applied axial load during the creep stages, as this was chosen as 30% of the failure stress for each sample. So, to facilitate comparison among zones, Fig. 13 presents the evolution of the compliance, taken as the evolving strain, ε, divided by the axial deviatoric stress applied during the creep stages, σ.

$$J = \frac{\varepsilon}{\sigma} \tag{2}$$

Recall also Fig. 13 takes the reference point for all strain values at the end of the hydrostatic phase, thus giving the graph for each sample a starting point of zero strain prior to application of the first deviatoric axial load. It is instructive to look in some detail at the behavior of each of the zones in Fig. 13.

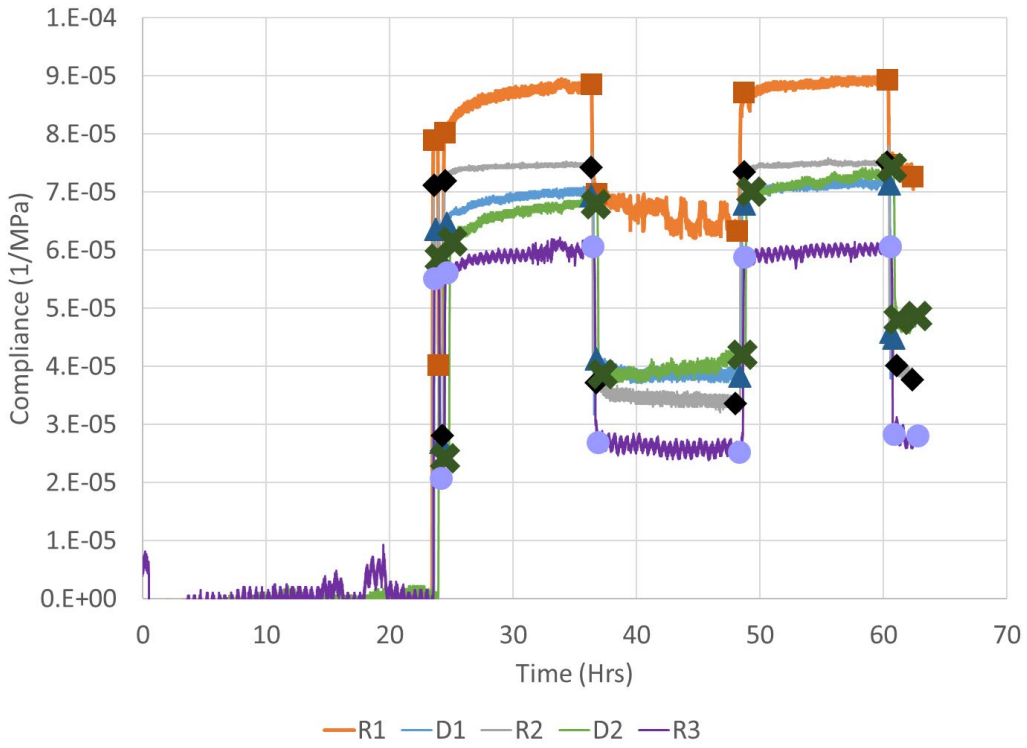

Fig. 13 Evolution of compliance (total axial strain divided by deviatoric stress) from creep tests

Reservoir 1

This zone has the largest total compliance at all points in the evolution of this quantity. After the initial 20-minute loading (seen at the 24-hour mark), about 50% of the strain was immediately recovered, indicating about 50% of the strain associated with the immediate deformation was plastic and 50% was elastic. On subsequent loading, the compliance returns to the same level and then undergoes substantial creep. Of this, about 40% is immediately recovered (indicating some additional immediate plastic deformation on the second loading) and in total around 50% is finally recovered at the end of the extended recovery period (ending at around 48 hours). In fact, the time-dependent compliance recovery (~0.5×10^{-5} 1/MPa) comprises around 50% of the total creep compliance (~1.0×10^{-5} 1/MPa), indicating a 50/50 split between viscoplastic and viscoelastic creep. In the final stage of loading, the compliance returns to a level suggesting there is no additional immediate plasticity, and the creep appears to be consistent with mostly viscoelastic deformation, with only a slight increase in the compliance level at the commencement of the final unloading indicating a small amount of viscoplastic deformation during the final creep stage.

Reservoir 2

At the outset one notices the compliance is the second largest, second only to Reservoir 1. However, the initial load/unload steps indicate over 50% is immediate plastic strain. Upon reloading and subjecting the sample to creep conditions, the compliance rapidly stabilizes and undergoes almost no change for the remainder of the stage. Upon unloading there is a small recovery, similar in magnitude to the creep which was previously sustained, indicating a viscoelastic mechanism. The final creep stage produces exactly the same compliance as the first, again with almost no increase over time. Hence, Reservoir 2 shows the most stable behavior with time and is the least susceptible to creep deformation.

Reservoir 3

Reservoir 3 exhibits the least compliance overall and a 70/30 split between elastic and plastic immediate deformation. Similar to Reservoir 2, the creep stages generate only a small amount of time-dependent deformation, essentially all of which is recovered indicating a viscoelastic mechanism. Although the total compliance is less than Reservoir 2, there is slightly more creep compliance on the longer time frames (as shown in more detail below).

Ductile 1 and Ductile 2

The behavior of these two zones is similar, with similar values of compliance at all stages of loading, despite the first ductile zone being approximately 100 feet above the second ductile zone. In both cases, the initial load/unload suggests a ~60/40 split between elastic and plastic immediate deformation. Both samples undergo significant creep with almost no recovery during the extended recovery stage. Hence, the creep is likely accommodated almost entirely as viscoplastic creep, with a negligible viscoelastic component.

Creep Compliance Calculation

In order to parameterize the creep compliance in a manner which can be implemented in numerical models, the immediate and time-dependent (creep) parts of the compliance are separated. The creep compliance for each zone is shown in Fig. 14a. Each zone is then fit with a power-law creep model,

$$J = \frac{\varepsilon}{\sigma} = J_{immed} + J_{cr} \qquad J = \mathrm{C} + kt^n \tag{2}$$

where C is the calculated compliance for the immediate part of the loading, t is the time in seconds since the differential load was applied, k is the coefficient in the creep law, and n is the time exponent in the creep law. Note when using a classical compliance coefficient typically denoted as B, the relationship to k is $k = B/\sigma$. Results of this fitting are shown in Table 2.

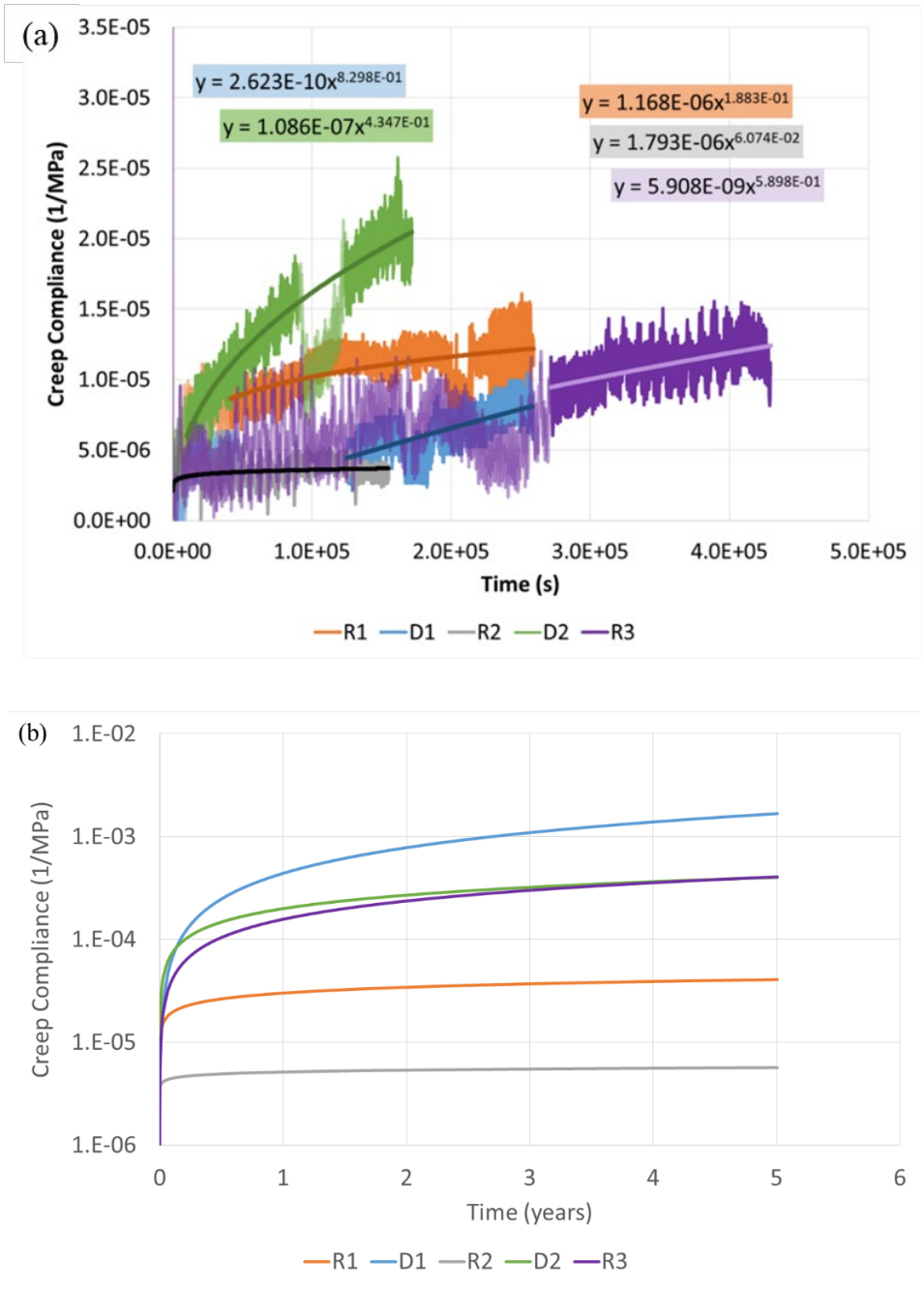

Fig. 14 (a) Creep compliance (axial creep strain divided by deviatoric stress) as a function of time, with power law fitted equations and (b) power law fit equations extended to five years

Table 2 Power-law creep model parameters, valid for stresses in MPa and time in seconds

Zone	k (1/MPa)	n (-)
Reservoir 1	1.17×10^{-6}	0.188
Ductile 1	2.62×10^{-10}	0.830
Reservoir 2	1.79×10^{-6}	0.061
Ductile 2	1.09×10^{-7}	0.435
Reservoir 3	5.91×10^{-9}	0.590

These results show Ductile 2 (D2) is the zone most susceptible to creep in the short term (Fig. 14). However, if the fitted creep law is projected out over a time frame of years, as shown in Fig. 14b, Ductile 1 emerges as the most prone to creep after approximately six months. In contrast, Reservoir 2 (R2) is the least susceptible to creep. As one might hypothesize for more clay-rich zones, the nominally ductile zones appear to have higher susceptibility to creep than the nominally brittle reservoir zones. These five-year extrapolations are based on laboratory testing, which by necessity is limited to a reasonable time frame, which in this case was 72 hours as this was the point when the axial strain appeared to reach a constant value. As with all other long-term creep estimations, a test spanning more than a year is unreasonable in terms of laboratory resources, and assumptions must be made for the creep of any material over long periods of time. However, these values were verified against the creep measured in the laboratory over the 72-hour loading stage, and the good agreement with measured strain values provides a fair confidence for extrapolating the strain beyond the time frame used in the laboratory.

5. Simulation of Proppant Embedment

Numerical modeling was performed to investigate the potential impact of shale creep on long-term proppant embedment and fracture closure. This modeling is part of ongoing work related to coupled multiphase fluid flow and geomechanical modeling of hydrocarbon production from a network of proppant-filled fractures. The necessary model developments and applications are based on the linking of the TOUGH2 multiphase fluid flow simulator with the FLAC3D geomechanical simulator (Pruess et al, 2012, Itasca, 2011, Rutqvist, 2011, and Rutqvist 2017). Focus is placed on the modeling of proppant embedment and fracture closure as a result of creep deformation over a five-year

time period. The simulations include the impact of elastic, plastic, and creep strain on proppant embedment and fracture closure. A Mohr-Coulomb model is applied to calculate plasticity and any plastic embedment which would occur as a result of the load taken by a proppant between closing fracture surfaces. Such a Mohr-Coulomb plasticity model has recently been applied to accurately model indentation experiments on shale (Voltolini et al, 2021, Katende et al, 2021b) and is therefore expected to be adequate for modeling elasto-plastic proppant embedment. For modeling creep embedment, an empirical power-law model was selected (Sone and Zoback, 2014, Rassouli, and Zoback, 2018). In this model, creep strain, ε_{creep} is calculated according to the expression

$$\varepsilon_{creep} = k\sigma_{vm}t^{n} \tag{3}$$

where σ_{vm} is von-Mises stress, *t* is time, and *k* and *n* are material properties. This creep model was selected because it has been successfully applied in previous work to analyze creep experiments on various shales (Sone and Zoback, 2014, Rassouli and Zoback, 2018, and Li and Ghassemi, 2012). As shown previously, the two model parameters *k* and *n* can be conveniently evaluated from triaxial creep tests using a graph of creep compliance versus time.

In this modeling, we consider two extremes of formation properties, namely Reservoir 2 representing nominally brittle reservoir properties and Ductile 1 representing a nominally ductile formation with high clay content. The power-law description of the creep deformation (Table 2) was used as the input for the creep properties of the formation during modeling, applying the elasto-plastic and creep properties as determined from core-scale triaxial compression and creep tests as described previously. The modeling is performed using an axisymmetric model, for an ideal case of spherical proppants of a certain diameter uniformly distributed in a monolayer (Fig. 15). The uniform proppant spacing, or center-to-center distance, between individual proppant particles are simulated by changing the radius of the axisymmetric model (Fig. 15b). The rollers in Fig. 15b illustrate boundaries where displacement is allowed parallel to the boundary surface while no displacement is allowed normal to the boundary. A stress corresponding to the fracture closure stress at depth is applied to the model in a direction normal to the fracture, which in Fig. 15b is from the bottom of the model. For the Caney shale it is reasonable to consider a fracture closure stress of 10,000 Psi (72 MPa) (after Vulgamore et al, 2021). Proppant diameters of 0.15 mm (150 μm) and 0.3 mm (300 μm) are considered to represent commonly used proppant mesh sizes for production from shale gas reservoirs. The 0.15 mm proppant diameter corresponds to a 100-mesh size proppant, whereas the 0.3 mm corresponds to an approximate average diameter for 40/70 mesh size proppant. The load taken by one proppant from the fracture closure

stress will depend on the spacing between neighboring proppants and will also depend on the reservoir fluid pressure. Here we consider an extreme case of complete pressure depletion during fluid production, meaning no stress is taken by fluid pressure but instead the stress normal to the fracture is funneled through the proppants.

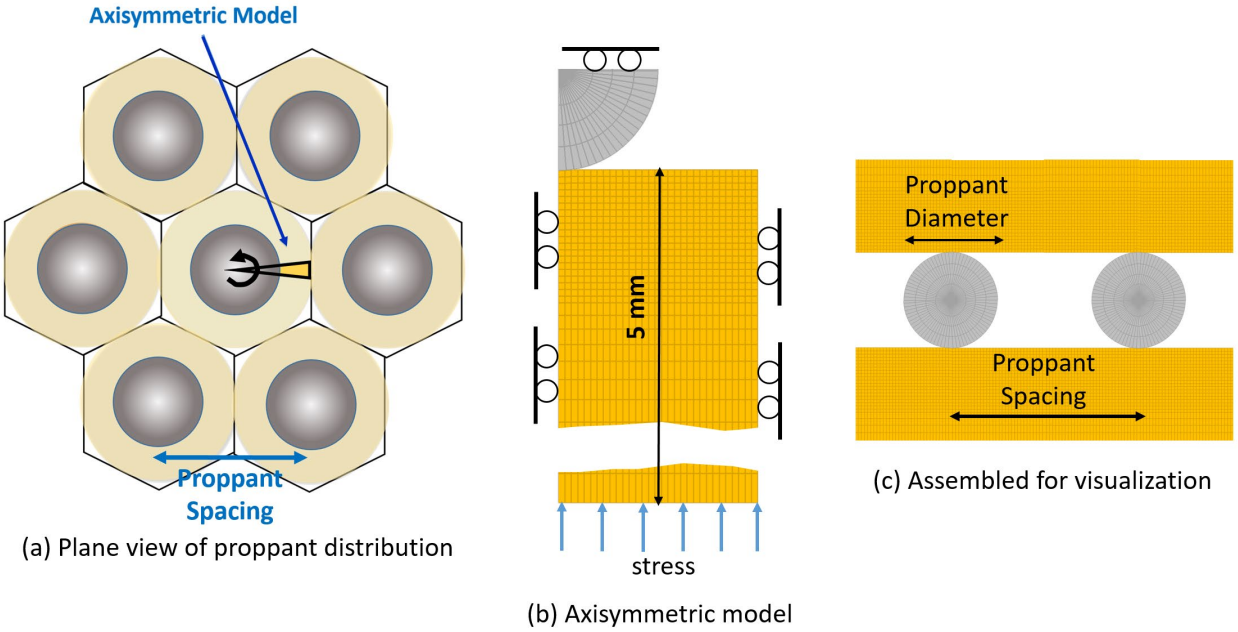

Fig. 15 Axisymmetric model geometry with boundary conditions and mesh discretization applied for modeling proppant embedment and fracture closure

Fig. 16 and Fig. 17 present modeling results of embedment for the idealized case of 0.15 mm (150 µm) diameter proppant located at a center-to-center distance of 0.3 mm in a monolayer of proppant. For the fracture closure stress of 10,000 psi (72 MPa), the average load on a proppant agent is estimated at 5.4 N for an extreme case of complete pressure depletion due to fluid production. Fig. 16 shows the evolution of proppant embedment, including the initial elasto-plastic embedment followed by time-dependent creep embedment during five years of constant proppant load. The model simulations show the amount of elasto-plastic creep embedment is much larger for Ductile 1 properties. The elasto-plastic embedment corresponds to a fracture closure of about 0.04 mm (40 µm) for Ductile 1 properties compared to only 0.025 mm (25 µm) for Reservoir 2 properties. Creep embedment is very different for the nominally ductile and nominally brittle formation properties. The creep closure amounts to only about 0.0002 mm (0.2 µm) for Reservoir 2, but as much as 0.064 mm (64 µm) for Ductile 1. Thus, we may conclude creep embedment is negligible in the case of the reservoir zone, whereas creep is significant in the case of the ductile zone. This confirms a correlation

between the clay content of a formation and its susceptibility for creep fracture closure. For the particular case studied, assuming 0.15 mm diameter proppant spaced 0.3 mm apart, the fracture would still be held open after five years even for the high-clay-content formation. The aperture at the mid distance between neighboring proppants after five years of creep is calculated as 0.125 mm for Reservoir 2 properties (Fig. 17a), and 0.05 mm for Ductile 1 properties (Fig. 17b). If flow through the fracture is proportional to the cube of the aperture (i.e., a classical cubic law from Poiseuille flow), then the reduction in conductivity of Ductile 1 would be around 16 times greater than Reservoir 2.

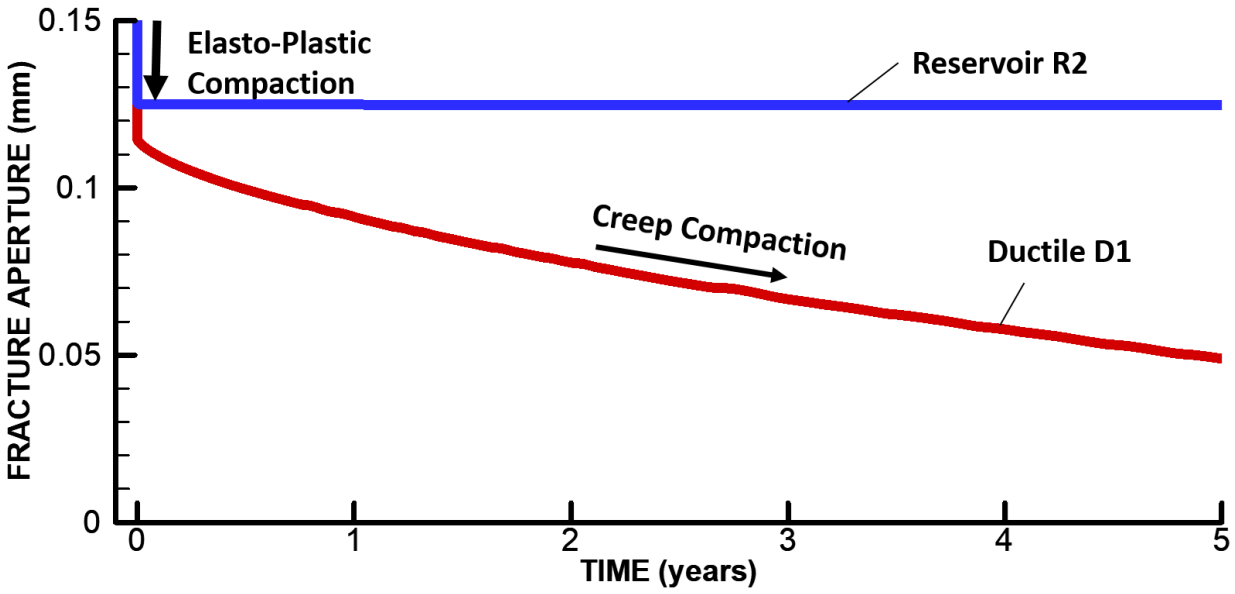

Fig. 16 Simulation results of elasto-plastic and creep compaction with calculated fracture aperture evolution as a results of proppant embedment for Reservoir 2 and Ductile 1 properties

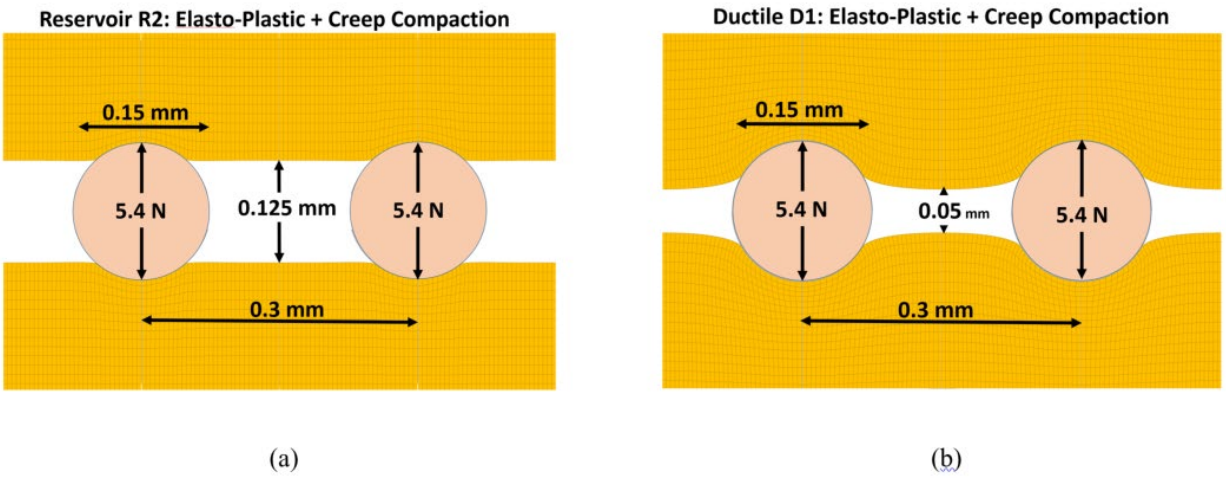

Fig. 17 Simulation results of proppant embedment after elasto-plastic and five years of creep compaction for (a) Reservoir 2 properties and (b) Ductile 1 properties

Fig. 18 and Fig. 19 present the results of sensitivity studies considering different proppant distances of 0.15, 0.30, and 0.40 mm apart, and two different proppant diameters of 0.15 and 0.3 mm. Recall the 0.15- and 0.3-mm proppant diameters correspond respectively to 100-mesh size and the average of 40/70 mesh size proppants. The proppant embedment depends strongly on the proppant spacing because the load taken by each proppant will increase with greater proppant spacing. For example, if the proppant spacing increases just from 0.3 mm to 0.4 mm, the proppant load would almost double from 5.4 to 9.6 N and the fracture would close completely after 2.4 years (Fig. 18a). On the other hand, if proppants are placed in perfect arrangement next to each other (i.e., distance 0.15 mm for 0.15 mm diameter proppants), the force taken by a proppant would be 1.4 N and the proppant embedment would be quite limited. However, the cross-sectional area open to flow through the propped fracture would be quite small, resulting in a relatively low fracture permeability. In the case of larger diameter (0.3 mm) proppants, the fracture aperture would not only be larger but, would also stay open longer for a given proppant distance. Considering a case for proppant spacing twice the proppant diameters, the relative permeability reduction will be similar but the absolute permeability would be higher in the case of the larger diameter proppants.

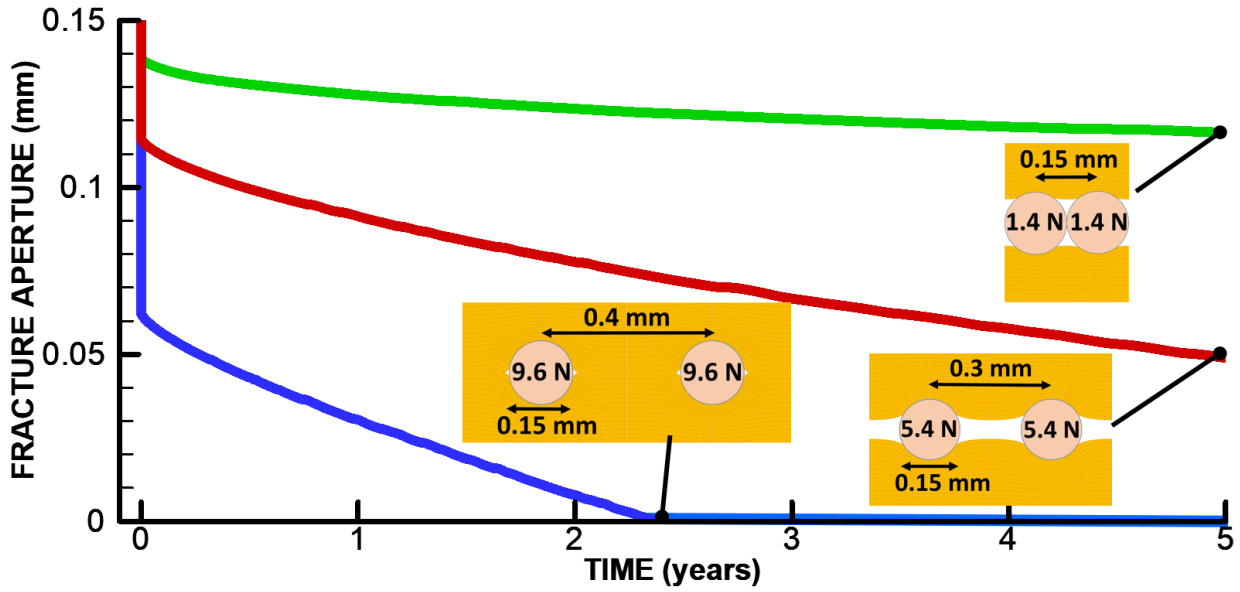

Fig. 18 Fracture opening width for Ductile 1 formation and 0.15 mm diameter proppant, plotted as a function of time with diagrams of final fracture geometry after 5 years of simulated time

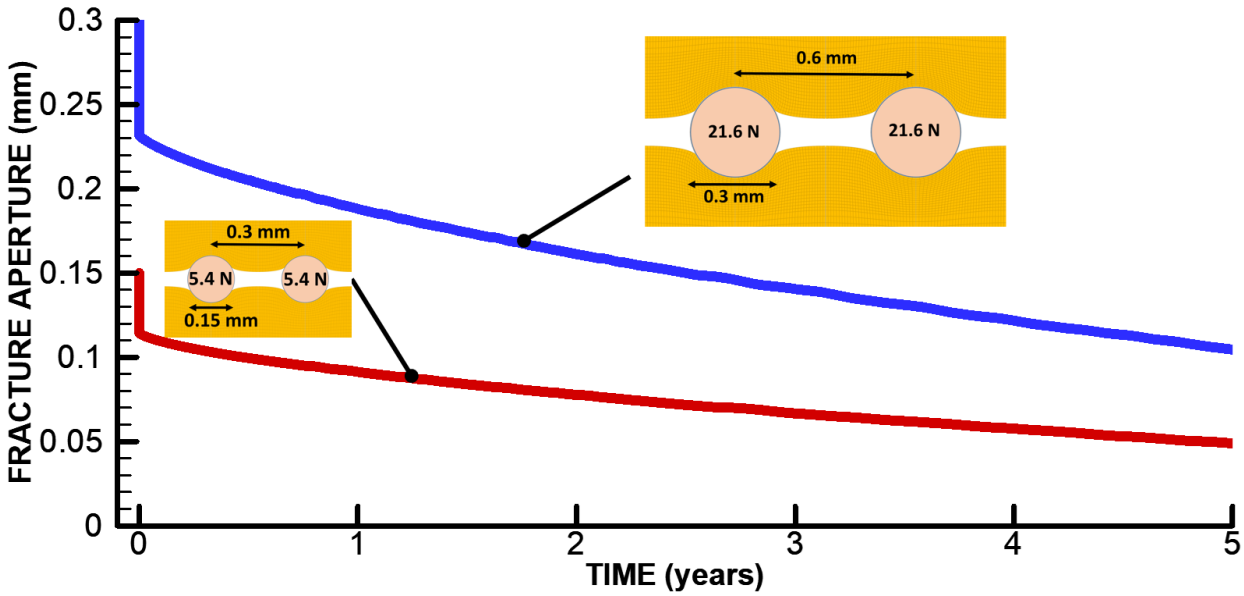

Fig. 19 Simulation results of two different proppant diameters (0.15 and 0.3 mm) and with proppant spacing twice the proppant diameter for the case of Ductile 1 properties

6. Discussion

An initial discussion point is the applicability of the terms “ductile” and “brittle” when describing the Caney shale samples. As previously demonstrated (Benge et al, 2021), these terms are potentially misleading when applied using the traditional geomechanical definitions of ductile and brittle. However, as has been demonstrated here, the ductile zones are mechanically weaker and more prone to long-term deformation in the form of creep. Therefore while the definition may not be strictly applicable, there is a usefulness in distinguishing the more creep-prone zones in the formation.

The second point worth discussing is the correlation between mechanical behavior of Caney samples from the five identified zones with their bulk composition as well as internal microstructure of each sample, primarily the difference between nominally ductile vs nominally brittle regions. It appears the clay rich zones are the most important mineralogical feature of Ductile 1 and 2 regions, while Reservoir 1, 2 and 3 are distinguished by high carbonate content (dolomite and calcite). The quartz content is similar in all zones. On the other hand, organic content is present in all zones, but Ductile 1 and 2 have finer, well-dispersed kerogen compared to larger, high-porosity kerogen lenses present in the reservoir zones. All of these observations support the mechanical testing data, as elasticity and creep are more associated with clays and fine-grained kerogen, while carbonates and large kerogen lenses would contribute to preferred fracturing, initiation and propagation. As demonstrated using the formation model, the nominally ductile zones tend to creep more than the nominally more brittle reservoir zones, which would cause fractures to slowly close due to creep. In terms of proppant embedment, embedment will occur more readily in clay-rich zones, while carbonate dissolution would contribute to weakening and fracture closure in reservoir zones, although this would be a slow and chemically driven process, rather than only by closing fracture stress. In this study we did not investigate the sample orientation in relation to the bedding of the rock, although bedding plane orientation would also play a role in how rock responds to the proppant embedment and ultimate fracture permeability in terms of production versus time. This study focuses only on the influence of creep and creep deformation on the long-term production of the well, and factors such as the permeability of the formation and amount of hydrocarbons present in the formation, while extremely important to determining overall production of a reservoir, are not the focus of this study. Additionally, this study does not examine the natural or unpropped fractures present in a formation, though it is likely the tendency of the formation to creep would have a significant impact on the productivity of these fractures.

Overall, the modeling shows creep embedment is negligible in the case of the most brittle reservoir zone, whereas creep is significant in the case of the ductile zone. This confirms a correlation between the clay content of a formation and its susceptibility for creep fracture closure. It also shows for ductile zones it is important to be able to place the proppants in a dense packing to avoid complete fracture closure. The simulated ductile zone demonstrated a tendency to creep closed much faster and to a greater extent than the nominally brittle reservoir zone, and therefore it can be concluded the nominally ductile zones would experience greater fracture closure and a corresponding greater drop in production over time compared to the nominally brittle zones. This difference in production may indicate a need to later re-stimulate any ductile zones which were fractured, and it may be possible to extract a greater volume of hydrocarbons overall from the nominally more brittle zones.

As the goal of this model simulation was to investigate the impact of shale creep on proppant embedment and fracture closure, other effects such as variable proppant shapes, proppant creep and crushing, and multilayer proppant placement have not been considered. For a thicker multilayer proppant pack (e.g., several mm thick), the fracture flow transmissivity will depend on the thickness and permeability of the proppant pack (e.g., unconsolidated sand permeability). A fracture closure on the order of 0.1 – 0.2 mm as calculated in this study would have a negligible impact on the fracture transmissivity compared a several millimeter thick proppant pack, where the particles of more central layers of proppant would support the particles closer to the formation, preventing full closure of the fracture. The multilayer proppant pack is more likely to occur near the well, while proppants emplaced in monolayers at variable proppant spacing are more likely to occur deeper into the stimulation zone away from the wellbore.

As a cautionary note, this paper focuses only on fracture closure due to proppant embedment (which may be both near-wellbore and far field), without accounting for factors such as the impact of fracturing fluids on the mechanical properties of the formation. While additional impacts are possible, the most obvious impact could be the swelling of clay components in the presence of water. This swelling could significantly increase the amount of proppant embedment. A second example of the impact of creep is provided by Sone and Zoback (2014), noting a large difference between maximum and minimum stresses in brittle formations and a nearly equivalent stress state in more ductile formations. This closure of the gap between stresses may be related to the increased creep tendency in ductile formations, and the increase in stresses may cause additional proppant embedment.

In addition to the closure of fractures in the formation, the change in the stress profile as predicted by Sone and Zoback (2014) is different than the traditional profile as calculated by Eaton's method (Eaton, 1969). The second method relies on the overburden pressure, depth of the formation, and Poisson's ratio, while Zoback's method leans heavily on the properties as determined from laboratory creep testing. While outside the scope of this paper, an examination of the measured in-situ stresses would indicate which of these methods provides an improved estimation of in-situ stresses. Changes in in-situ stresses between layers would cause an issue when stimulating the formation, as fractures grow preferentially in low-stress formations. Again, while the specifics of designing a stimulation plan are outside the scope of this document, the additional control mechanisms required to ensure fracture growth in targeted areas should be considered when designing a well for hydrocarbon extraction.

Sone and Zoback (2014) also discuss assigning brittleness grades which vary with changes in in-situ stresses and mineral composition. Another example from Kainer et al (2017) examining rock fabric factors noted a positive trend between Young's modulus and Brinell hardness with fracture conductivity, but recognized other factors appear to contribute to conductivity. Zhang et al (2014) examined the relationships of brittleness and ductility to fracture conductivity and concluded the conductivity of an unpropped fracture is directly related to brittleness while the conductivity of a propped fracture shows a weak correlation to the elastic properties of the shale samples. Similarly, this study did not find a clear correlation between the Young's modulus and the power-law creep properties as determined from laboratory testing. Thompson et al. (2010) introduced the concept of production hindrance in the ductile Haynesville formation and linked the deformation of formations under "highest effective stress" and proppant embedment in the near wellbore as an "irreversible conductivity choke", suggesting the gradual application of stress in controlled drawdowns could decrease the decline in production by 50% or more.

One final reminder is required noting the highly variable nature of rocks. This study, as with any study based on experiments which require a long time to perform, is necessarily limited to testing of a few samples, and simulations were performed to supplement the limited number of laboratory data points. This is the classical and ubiquitous issue of representative properties in rock mechanics, and it is to be respected here owing to the potential for wide variances existing in the rock fabric of the rock formations of interest. While a more detailed description of the properties of the Caney shale will be provided using an increased data set from planned future testing, the number of samples tested in

this, and any practically achievable testing plan, is always smaller than what would be needed to fully characterize variability of actual rock formations, especially in complicated sedimentary basins.

7. Conclusions

As an emerging hydrocarbon play, the Caney shale was previously thought to be a relatively ductile shale formation, with some zones identified on well logs as more ductile than others. The classification based on the well log is successful in identifying the nominally brittle and nominally ductile formations as correlated to mineralogy. Ductile zones are correctly identified as zones with higher clay content and smaller quartz-feldspar content than the identified nominally brittle reservoir zones. However, past work has shown "brittle" and "ductile" are not strictly applicable to describe the differences in mechanical behavior in the identified zones.

Nevertheless, the well log and mineralogy are shown in this study to be capable of identifying zones which are weaker and more prone to creep deformation over time. Indeed, we show the nominally ductile zones consistently fail at lower stresses compared to the nominal reservoir zones. Additionally, the lowest value of the Young's modulus and the lowest friction angle are associated with the zone which is also the most prone to creep deformation. The two nominally ductile zones are substantially more prone to creep with 5-year creep compliance values around 100 times larger than the least creep-prone of the nominal reservoir zones. However, when using traditional triaxial testing methods there was not a clear correlation between triaxial properties such as Young's modulus and Poisson's ratio and the power-law used to describe creep behavior, only the qualitative one described. This could in part be due to the methods used to obtain samples, as by necessity the core was exposed to ambient conditions and stresses induced by tectonic influences such as the pressure in the formation could have relaxed and altered the properties of the samples.

Hence, the experiments show how, from the perspective of creep deformation, there is a clear difference between the ductile and reservoir zones. This higher susceptibility of ductile zones to creep deformation can be expected to translate into a higher tendency for proppant embedment which, in turn, lowers the hydraulic aperture of propped hydraulic fractures and can lead to production decline. Numerical simulations show the long-term proppant embedment associated fracture closure and fracture permeability is significantly influenced by the lower strength and higher creep compliance of the nominally ductile zones compared to the nominally brittle zones. Specifically, the reservoir zones undergo negligible creep while ductile zones can be expected to undergo creep-driven proppant

embedment leading to loss of fracture aperture ranging up to 100% loss, depending upon the spatial density of the proppant distribution. Hence, this research shows the identification of nominal "ductile" zones from well logs, while a misnomer, can be useful in finding clay-rich, creep-prone zones which will be the most prone to proppant embedment and hence vulnerable to greater production decline over time. This insight into the behavior of the formation allows for optimization of the stimulation plan, targeting zones which will not experience a significant decline in production due to fracture closure and potentially performing additional treatments as needed to improve the overall hydrocarbon extraction.

While the experiments and simulations are specific to the Caney shale, there are several principles which could be applicable to other shale reservoirs. Most notably, despite the misnomer, identifying nominally "ductile" zones based on well logs is beneficial to provide an indication of layers which will be more susceptible to proppant embedment and can be expected to experience more significant production decline compared to nominally brittle "reservoir" zones. With this said, the utility of such an approach has been shown for comparison among layers within a given formation, and it is not clear whether one can meaningfully use such correlations to speculate about the economic prospects of a new formation based on comparison to a different play. Nonetheless, the relationship among log properties, mineralogy, microstructure, strength, and creep susceptibility illustrates an integrated approach to shale evaluation which, with the help of geomechanical simulations, gives a comprehensive view of physical and mechanical properties of the shales and the potential for these properties to meaningfully impact production for various zones within a target formation.

8. Supporting Data

Data used to generate figures is available in the data compendium at:

http://d-scholarship.pitt.edu/id/eprint/44094

Acknowledgements

Support is provided by the United States Department of Energy's Office of Fossil Energy and Carbon Management under Cooperative Agreement DE-FE0031776 and DE-AC02-05CH11231, with Joe Renk serving as the officer overseeing this project. Thank you to Continental Resources for additional support for this project and for permission to publish, in particular to Andy Rihn and Brian Kilian. Partial support for APB is provided by the R. K. Mellon

Faculty Fellowship in Energy. UCS results and core plugging were provided by Eric Cline, formerly with Chesapeake Energy. The authors also wish to acknowledge Mr. Brent Johnson and Mrs. Lisa Whitworth at the OSU Venture 1 Microscopy Facility for training in using the equipment. Dustin Crandall and his team at National Energy Technology Laboratory provided the core photographs and X-ray CT images. Thank you also to Yunxing Lu and Charles Hager at University of Pittsburgh for their assistance with experiments and to Adam Haecker and George King for helpful discussions of this work.

This paper is conceptually based on Benge et al. (2021, URTeC 5084) in its structure and motivation to show connections among petrophysics, microstructure/composition, mechanical properties, and propensity for proppant embedment. However, all results presented here are new and discussions have been expanded and modified nearly in their entirety. The results presented here should be considered to supersede the more preliminary results presented in URTeC 5084.

Compliance with Ethical Standards

Support is provided by the United States Department of Energy's Office of Fossil Energy and Carbon Management under Cooperative Agreement DE-FE0031776 and DE-AC02-05CH11231. Partial support for A. Bunger is provided by the R. K. Mellon Faculty Fellowship in Energy. The authors have no other relevant financial or non-financial interests to disclose.

References

ASTM D7012-14. 2014. Standard Test Methods for Compressive Strength and Elastic Moduli of Intact Rock Core Specimens under Varying States of Stress and Temperatures. ASTM International.

Awejori, G.A., Doughty, C., Spycher, N. Paronish, T. Radonjic, M., Geochemical Reactions of Simple Fracturing Fluids with Caney Shale, Energy Fuels 2022, 36, 17, 10064–10081, August 22, 2022.

Awejori, G.A., Luo, G., Grider, C., Katende, A., Radonjic, M. Doughty, C., Spycher, N. Paronish, T. O'Connell, L. Rihn, A. 2021. Fracturing Fluid-Induced Mineralogy Changes and Impact on Elastic Properties for the Caney Shale, Oklahoma. Presented at the 55th US Rock Mechanics/Geomechanics Symposium, Houston, 18-25 June. ARMA-21-2004.Bai, M. 2016. Why are Brittleness and Fracability not Equivalent in Designing Hydraulic Fracturing in Tight Shale Gas Reservoirs. Petroleum 2.1: 1-19.

Bandara, K., Ranjith, P., and Rathnaweera, T. 2019. Improved understanding of proppant embedment behavior under reservoir conditions: A review study. Powder Technology, 352, 170-192.

Benge, M., Lu, Y., Jones, J., Bunger, A., Haecker, A., Rihn, A., Crandall, D., Luo, G., and Radonjic, M., 2020. Mechanical Properties of Nominally Ductile and Brittle Zones within the Caney Shale Formation. Presented at 55th US Rock Mechanics/Geomechanics Symposium, Houston, 18-25 June. ARMA 21-1570.

Benge, M., Lu, Y., Katende, A., Rutqvist, J., Crandall, D., Haecker, A., King, G., Renk, J., Radonjic, M., Bunger, A.P. 2021. Connecting Geomechanical Properties with Potential for Proppant Embedment and Production Decline for the Emerging Caney Shale, Oklahoma. Unconventional Resources Technology Conference (URTeC), Houston, Texas, 26-28 July 2021. UTReC 5084.

Cardott, B. 2017. Oklahoma Shale Resource Plays. Oklahoma Geology Notes 76.2 (2017): 21-30.

Eaton, B. 1969. Fracture Gradient Prediction and Its Application in Oilfield Operations. Journal of Petroleum Technology 21.10 (1969): 1353-1360.

Fadjarijanto, A., Rachmadi, A., Setiawan, A. S., Praptono, A., Suriyo, K., Simatupang, M., Pakpahan, O., Costam, Y. and Zakaria, Z. 2018. "Three Petrophysics Techniques Applied for the Thin Lamination Reservoir: The Impact towards Significant Reserve Addition." Paper presented at the Offshore Technology Conference Asia, Kuala Lumpur, Malaysia, March 2018.

Frash, L., Hampton, J., Guiterrez, M., Tutuncu, A., Carey, J., Hood, J., Mokhtari, M., Huang, H., and Mattson, E. 2019. Patterns in Complex Hydraulic Fractures Observed by True-Triaxial Experiments and Implications for Proppant Placement and Stimulated Reservoir Volumes. Journal of Petroleum Exploration and Production Technology 9.4 (2019): 2871-2792.

Itasca. 2011. FLAC3D v5.0, Fast Lagrangian Analysis of Continua in 3 Dimensions, Users Guide.

Kainer, C., Guerra, D., Zhu, D., Hill, A. 2017. A Comparative Analysis of Rock Properties and Fracture Conductivity in Shale Plays. Paper presented at the SPE Hydraulic Fracturing Technology Conference and Exhibition, The Woodlands, Texas, USA, January. SPE-184877.

Katende A., Allen C., Rutqvist J., Nakagawa S., and Radonjic M. Experimental and numerical investigation of proppant embedment and conductivity reduction within a fracture in the Caney Shale, Southern Oklahoma, USA. Fuel 341, 127571 (2023). https://doi.org/10.1016/j.fuel.2023.127571.

Katende, A., O'Connel, L., Rich, A., Rutqvist, J., and Radonjic, M., (2021a). A Comprehensive Review of Proppant Embedment in Shale Reservoirs: Experimentation, Modeling and Future Prospects. Journal of Natural Gas Science and Engineering, 95, 104143 2021.

Katende, A., Rutqvist, J., Benge, M., Seyedolali A., Bunger, A., Puckette J.O., and Radonjic, M. 2021b. Convergence of Micro-Geochemistry and Micro-Geomechanics Towards Understanding Proppant Shale Rock Interaction: a Caney Shale Case Study in Southern Oklahoma, USA. Journal of Natural Gas Science and Engineering,96, 104296 2021.

Kovari, K., Tisa, A., Einstein, H. H., & Franklin, J. A. (1983). Suggested Methods for Determining the Strength of Rock Materials in Triaxial Compression: Revised Version. Intl J of Rock Mech & Mining Sci & Geomechanic Abs, 20(6).

Li, Y., and Ghassemi, A. 2012. Creep Behavior of Barnett, Haynesville, and Marcellus Shale. 46th US Rock Mechanics / Geomechanics Symposium 2012, 1, 641–647.

Loucks, R. G., Reed, R. M., Ruppel, S. C., & Hammes, U. (2012). Spectrum of Pore Types and Networks in Mudrocks and a Descriptive Classification for Matrix-Related Mudrock Pores. AAPG bulletin, 96(6), 1071-1098.

Pruess, K., Oldenburg, C., and Moridis, G. 2012. TOUGH2 User's Guide Version 2.1, Report LBNL-43134. Lawrence Berkeley National Laboratory, Berkeley, CA, USA.

Radonjic, M., Luo, G., Wang, Y., Achang, M., Cains, J., Katende, A., Puckette, J., Grammer, M., and King, G. 2020. Integrated Microstructural Characterization of Caney Shale, OK. Presented at 2021 Unconventional Resouces Technology Conference, Houston, 26-28 July. URTeC 2947.

Rassouli, F., and Zoback, M. 2018. Comparison of Short-Term and Long-Term Creep Experiments in Shales and Carbonates from Unconventional Gas Reservoirs. Rock Mechanics and Rock Engineering 51: 1995 – 2014.

Rickman, R., Mullen, M., Petre, E., Grieser, B., and Kundert, D. 2008. A Practical Use of Shale Petrophysics for Stimulation Design Optimization: All Shale Plays Are Not Clones of the Barnett Shale. Presented at the 2008 SPE Annual Technical Conference and Exhibition, Denver, Colorado, 21-24 September. SPE-115258.

Rutqvist J. 2011. Status of the TOUGH-FLAC Simulator and Recent Applications Related to Coupled Fluid Flow and Crustal Deformations. Computers & Geosciences 37: 739–750.

Rutqvist, J. 2017. An Overview of TOUGH-Based Geomechanics Models. Computers & Geosciences 108: 56–63.

Sone, H., & Zoback, M. 2014. Time-Dependent Deformation of Shale Gas Reservoir Rocks and its Long-Term Effect on the In Situ State of Stress. International Journal of Rock Mechanics and Mining Sciences 69: 120-132.

Thompson, J. W., Fan, L., Grant, D., Martin, R. B., Kanneganti, K. T., and G. J. Lindsay. 2010 An Overview of Horizontal Well Completions in the Haynesville Shale. Paper presented at the Canadian Unconventional Resources and International Petroleum Conference, Calgary, Alberta, Canada, October 2010.

Voltolini, M., Rutqvist, J., and Kneafsey, T. 2021. Coupling Dynamic in Situ X-Ray Micro-Imaging and Indentation: A Novel Approach To Evaluate Micromechanics Applied To Oil Shale. Fuel 300: 120987.

Vulgamore, T., Wolhart, S., Mayerhofer, M., Clawson, T. and Pope, C. 2008. Hydraulic Fracture Diagnostics Help Optimize Stimulations Of Woodford Shale Horizontals. The America Oil&Gas Reporter April 15 (2008).

Wang, Y., Luo, G., Achang, M., Cains, J., Wethington, C., Katende, A., Grammer, G. M., Puckette, J., Pashin, J., Castagna, M., Chan, H., King, G. E., & Radonjic, M. (2021). Multiscale Characterization of the Caney Shale — an Emerging Play in Oklahoma. Midcontinent Geoscience, 2, 33–53.

Xiong F., Rother, G., & Radonjic, M., Insights into controls of mineralogy and pore structure on the density of adsorption phase in shales under supercritical conditions, Energy Fuels 2022, 36, 17, 10110–10122, August 22, 2022.

Zhang, J., Kamenov, A., Zhu, D., and Hill, A. 2014. Laboratory Measurement of Hydraulic-Fracture Conductivities in the Barnett Shale. SPE Production & Operations 29 (2014): 216-227.